

University of Dundee

Bore pressure on horizontal and vertical surfaces

Liu, Jiaqi; Hayatdavoodi, Masoud; Cengiz Ertekin, R.

Published in:

Proceedings of the International Conference on Offshore Mechanics and Arctic Engineering - OMAE

DOI:

[10.1115/OMAE2019-96013](https://doi.org/10.1115/OMAE2019-96013)

Publication date:

2019

Document Version

Peer reviewed version

[Link to publication in Discovery Research Portal](#)

Citation for published version (APA):

Liu, J., Hayatdavoodi, M., & Cengiz Ertekin, R. (2019). Bore pressure on horizontal and vertical surfaces. In *Proceedings of the International Conference on Offshore Mechanics and Arctic Engineering - OMAE* (Vol. 7a). [V07AT06A008] American Society of Mechanical Engineers. <https://doi.org/10.1115/OMAE2019-96013>

General rights

Copyright and moral rights for the publications made accessible in Discovery Research Portal are retained by the authors and/or other copyright owners and it is a condition of accessing publications that users recognise and abide by the legal requirements associated with these rights.

- Users may download and print one copy of any publication from Discovery Research Portal for the purpose of private study or research.
- You may not further distribute the material or use it for any profit-making activity or commercial gain.
- You may freely distribute the URL identifying the publication in the public portal.

Take down policy

If you believe that this document breaches copyright please contact us providing details, and we will remove access to the work immediately and investigate your claim.

BORE PRESSURE ON HORIZONTAL AND VERTICAL SURFACES

Jiaqi Liu

Civil Engineering Department
University of Dundee
Dundee, DD1 4HN, UK
Email: joliu@dundee.ac.uk

Masoud Hayatdavoodi

Civil Engineering Department
University of Dundee
Dundee, DD1 4HN, UK
Email: mhayatdavoodi@dundee.ac.uk

R. Cengiz Ertekin

Ocean and Resources Engineering Department
University of Hawaii at Manoa
Honolulu, Hawaii, USA
Email: erteikin@hawaii.edu

ABSTRACT

Bores generated by dam-break and initial mound of water and their propagation over horizontal and inclined surfaces are studied by use of theoretical approaches. Calculations are carried out in two and three dimensions and particular attention is given to the bore impact on horizontal and vertical surfaces. Downstream of the initial mound of water may be wet or dry. Discussion is provided on the influence of the downstream water on the bore behaviour and impact. Three methods are used in this study, namely the Reynolds-Averaged Navier-Stokes equations (RANS), the Green-Naghdi (GN) equations and Saint Venant equations (SV). The governing equations subject to appropriate boundary conditions are solved with various numerical techniques. Results of these models are compared with each other, and with laboratory experiments when available. Discussion is given on the limitations and applicability of these models to study the bore generation, propagation and pressure on horizontal and vertical surfaces. It is found that the GN equations compare well with the RANS equations, while the SV equations have substantially simplified the solution.

Keywords: Dam break, initial mound of water, Reynolds-Averaged Navier-Stokes equations, Green-Naghdi equations, Saint Venant equations

Introduction

Bore is generated due to the collapse of a block of fluid. The block of fluid maybe initially at rest (in the case of bores generated by collapse of a reservoir) or in the form of a stable moving wave (in the case of bores generated by solitary wave breaking). Bore dynamic depends on the generation mechanisms and characteristics, and the downstream conditions. Dam-break and initial mound of water are two examples of bore generation due to a reservoir. The difference between these two cases is the level of the downstream water depth, which results in different bore behaviours.

Propagation of water surging over dry or wet beds is studied as dam-break problems. Examples of dam-break problems are the flash flood caused by dam failure, debris flow surges and tsunami bore runup on a dry coast. Due to the large inertia and impact of the sudden interaction of the body of fluid with structure in a dam-break, immense damages may occur.

There are many examples of the vast damages made by dam-break impact. On December 1, 1923, one buttress of the Gleno Dam in Italy was destroyed and about $4500000m^3$ of water rushed out from the reservoir behind the dam from an elevation about 1535m above the sea level to the valley below. 356 lives were lost in this disaster, see Pilotti *et al.* (2010) [1]. On June 5, 1976, due to the piping and internal erosion at the foot of the Teton Dam in the United States, the right-bank of the main dam wall disintegrated. At a flow rate of $57000m^3/s$, muddy water run off the reservoir into

the Teton River canyon. The damage was estimated at 2 billion USD and 11 people died in this disaster, see Seed and Duncan (1981) [2]. Due to the epicentre off the west coast of Sumatra, Indonesia, on 26 December 2004, a series of devastating tsunamis, with a height about 30m, arrived at coastal communities, see Yalciner *et al.* (2005) [3]. With about 250000 killed in 14 countries, the tsunami is recorded as one of the deadliest natural disasters in the history, see West, Sánchez and McNutt (2005) [4].

Perhaps one of the first studies on dam break flows is that of Ritter (1892) [5], who introduced theoretical solution of dam break flows based on his shallow water theory. More recently, numerous studies on dam break flows have been carried out, but the dynamics of dam break flows have not been thoroughly studied before 1999. The constrained interpolation profile (CIP) method is adopted by Hu and Masashi (2004) [6] for their CFD model to study the pressure on the downstream wall of a dam-break case. The numerical simulation results of pressure are compared with experiments. Good agreement is achieved by their CIP-based method. Zhou *et al.* (1999) [7] present a series of numerical results, based on Glimm's method, of dam-break pressure. Kleefsman *et al.* (2005) [8] studied the problem by use of volume of fluid method to determine the pressure closer to the horizontal bed. Wemmenhove *et al.* (2010) [9] carried out a similar study but their simulations are focused on examining sloshing physics. Dam-break experiments are carried out by Lobovský *et al.* (2014) [10] to study the bore propagation and magnitude of the pressure on the downstream wall.

Another form of bore generation is due to the breaking of an initial mound of water. The fundamental difference between dam-break and initial mound of water is due to the ratio of the reservoir depth to the downstream water depth. In the dam-break problems, this ratio is larger than (approximately) while this ratio is smaller than 2 for the initial mound of water. This difference in downstream water depth results in different form of flow generation downstream of the reservoir. In this work, we will study both types of bores, generated by dam-break and by an initial mound of water.

Although many works have been done on estimating the bore pressure distribution, the descriptions of that of bore on the downstream wall are still not very clear. It is important to find an appropriate model which can calculate the bore pressure correctly, both in engineering and scientific applications.

This study is concerned with the calculation of bore generation and pressure on the horizontal floor and vertical walls. Three theoretical approaches are used to study this problem, including the Reynolds-Averaged Navier-Stokes equations, the Green-Naghdi equations and the Saint Venant equations. Our goal is to determine whether these models can provide acceptable results of the bore propagation and pressure, and to provide discussion on their limitations and restrictions.

The Theories

Three sets of equations are used in this study, namely the Reynolds-Averaged Navier-Stokes (RANS) equations, the Green-Naghdi (GN) equations and the Saint Venant (SV) equations. These are discussed in this section. We adopt a right-handed 3-D Cartesian coordinate system, with x_1 pointing to the right, x_2 pointing vertically opposite to the direction of the gravitational acceleration ($x_2 = 0$ corresponds to the sea-floor), and x_3 pointing into the paper. Indicical notation and Einstein's summation convention are used. Subscripts after comma indicate differentiation.

Reynolds-Averaged Navier-Stokes Equations

For a homogeneous, Newtonian and incompressible fluid, the three dimensional RANS equations are given by the following conservation of mass and momentum equations:

$$\bar{u}_{i,i} = 0, \quad i = 1, 2, 3 \quad (1)$$

$$\bar{u}_{j,t} + (\bar{u}_i \bar{u}_j + \overline{u'_i u'_j})_{,i} = g_j - \frac{1}{\rho} \bar{p}_{,j} + \nu \bar{u}_{j,ii}, \quad i, j = 1, 2, 3 \quad (2)$$

where $\bar{f}(x_1, x_2, x_3, t)$ is the time-averaged value of the fluctuation value, $\bar{\mathbf{u}} = u_i \bar{\mathbf{e}}_i$ is the velocity vector, and $\bar{\mathbf{e}}_i$ is the unit normal vectors in the i direction. ρ is the density of fluid, ν is kinematic viscosity, $\bar{\mathbf{g}} = (0, -g, 0)$ is the gravitational acceleration and p is the pressure.

There are two commonly used turbulence models for the RANS equations, namely, the $k - \omega$ model and the $k - \varepsilon$ model. There are two advantages of the $k - \omega$ for the bore impact problems: the model is applicable to variable pressure gradients, and it is more sensitive to free surface problems, see *e.g.* Wilcox *et al.* (1988) [11]. The pressure on the downstream wall is sensitive to the shape of the bore, see Mokrani and Abadie (2016) [12]. We adopt a $k - \omega$ model in this study for the turbulence closure.

In the $k - \omega$ model, the kinematic viscosity is assumed to be related to the turbulent kinetic energy and dissipation. Menter (1993) [13] introduced the relation as

$$\nu_t = \frac{\omega}{\rho k}, \quad (3)$$

where ν_t is the eddy-viscosity, k is the thermal conductivity and ω is the specific turbulence dissipation rate. The value of ω is related to the turbulence kinetic energy and turbulence dissipation rate, See Menter (1993) [13] and Menter, and Kuntz and Langtry (2003) [14] for more details on the $k - \omega$ model used here.

Volume of Fluid method (VOF method), originally introduced by Hirt and Nichols (1981) [15], is used to determine the free surface between air and water. A scale function is used to represent the volume of fluid in each cell, see

Hirt and Nichols (1981) [15].

OpenFOAM is used for the computations of the RANS equations. Boundary conditions used in this study are presented in Table 1. Details of these boundary conditions can be found in *e.g.* Greenshields (2018) [16] and Higuera, Lara and Losada (2013) [17].

The Green-Naghdi Equations

The GN equations are originally derived by use of the directed fluid sheet theory introduced by Green, Laws and Naghdi (1974) [18], and Green and Naghdi (1976) [19]. They are applicable to unsteady, nonlinear flows of inviscid and incompressible fluids. The GN equations satisfy the nonlinear boundary conditions exactly, and postulate the integral balance laws. Green and Naghdi [20] showed that the GN equation can be obtained from the exact 3-D governing equations of an incompressible and inviscid fluid by making a single assumption about the distribution of the vertical velocity along the fluid sheet. The resulting equations satisfy exactly the nonlinear boundary conditions, the mass conservation, and the integrated momentum and moment of momentum, see *e.g.* Ertekin (1985) [21] for details. The GN equations are classified based on their levels, corresponding to the function used for the distribution of the vertical velocity along the water column. In this study, we use the Level I the GN equations (or the original GN equations). A linear distribution of vertical velocity is assumed in the level I equations.

The GN equations are use here in two dimensions and in the form first given by Ertekin (1984) [21]:

$$\zeta_t + [(h + \zeta - \alpha)u_1]_{,1} = 0, \quad (4)$$

$$\begin{aligned} \dot{u}_1 + g\zeta_{,1} + \frac{\hat{p}_{,1}}{\rho} = & -\frac{1}{6}[(2\zeta + \alpha)_{,1}\ddot{\alpha} \\ & + (4\zeta - \alpha)_{,1}\ddot{\zeta} \\ & - (h + \zeta - \alpha)(\ddot{\alpha} + 2\ddot{\zeta})_{,1}], \end{aligned} \quad (5)$$

where ζ is the free surface elevation measured from the still water level (SWL), α is the elevation of the bottom surface, and \hat{p} is the pressure on the top surface of the fluid sheet. The superposed dot denotes the material time derivative, and double dot is the second order material derivation.

The GN equations have been applied to many problems of unsteady flow impact on structures, see *e.g.* Hayatdavoodi and Ertekin (2015) [22–24] for impact on horizontal surfaces, and Neill *et al.* (2018) [25] and Hayatdavoodi *et al.* (2018) [26] for impact on vertical surfaces.

Saint-Venant Equations

The SV equations, whose 3-D form is called Shallow Water equations, are derived from Eqs. (1) and (2) with three

assumptions: (i) the viscous terms are negligible, (ii) pressure is assumed hydrostatic, and (iii) the fluid flows in one dimension only (x_1 direction), where u_2 is small enough to be omitted, and u_1 is assumed to be constant in x_2 -direction. In the absence of viscous terms, the effect of viscosity is considered by use of empirical terms and the body force. Hence the SV equations read as, (see Saint-Venant (1871) [27] and Mises (1945) [28]),

$$u_{1,t} + u_1 u_{1,1} = -gh_{,1} + gS - gS_f, \quad (6)$$

where h is the water depth, $S(x_1) = -\alpha_{,x_1}$ is the bed slope, $S_f(x_1, t) = \frac{\tau}{\rho g R}$ is the friction slope, $\tau(x_1, t)$ is the shear stress along the wetted perimeter $p(x_1, t)$ of the cross section at location x_1 and $R(x_1, t) = \frac{A}{p}$ is the hydraulic radius, where $A(x_1, t)$ is the cross-sectional area of the flow. The shear stress is given by Manning Equations, see Manning [29]. To determine the pressure, we use the unsteady Bernoulli equation.

For small-amplitude oscillations, the unsteady Bernoulli equation is given by (see *e.g.* Kundu and Cohen (1990) [30]):

$$\phi_t + \frac{p}{\rho} + g(h - x_2) = C, \quad (7)$$

where ϕ is the velocity potential, C is a constant, x_2 is the vertical height from the base ($x_2 = 0$) and p is the pressure. By substituting $d\phi = u_1 dx_1 + u_2 dx_2$ in Eq. (7), we obtain

$$\frac{\partial(\int u_1 dx_1 + \int u_2 dx_2)}{\partial t} + \frac{p}{\rho} + g(h - x_2) = C, \quad (8)$$

and hence the pressure is determined by:

$$p(x_1, x_2, t) = \rho g(h - x_2) + \rho \frac{\partial(\int u_1 dx_1 + \int u_2 dx_2)}{\partial t}. \quad (9)$$

Numerical Solutions

The three governing equations are solved numerically using various techniques. These are introduced here.

The RANS equations are solved by use of a finite-volume approach. The integral form of the RANS equations, Eqs. (1) and (2) over time and space can be writ-

TABLE 1: Boundary conditions used in the RANS model. For definition of the boundary conditions, see *e.g.* Greenshields (2018) [16] and Higuera, Lara and Losada (2013) [17].

Boundary	β	p	u
bottom	zeroGradient	zeroGradient	fixedValue (0,0,0)
left and right wall	zeroGradient	zeroGradient	fixedValue (0,0,0)
front and back wall	empty	empty	empty
atmosphere	inletOutlet	totalPressure	pressureInletOutletVelocity

ten as:

$$\begin{aligned}
 & \int_t^{t+\Delta t} \left[\iint \bar{u}_{j,i} dx_i dx_j + \iint (\bar{u}_i \bar{u}_j + \overline{u'_i u'_j})_{,i} dx_i dx_j \right] dt \\
 &= \int_t^{t+\Delta t} \left[\iint g_j dx_i dx_j \right. \\
 &\quad - \iint \frac{1}{\rho} \bar{p}_{,j} dx_i dx_j \\
 &\quad \left. + \iint \nu \bar{u}_{j,ii} dx_i dx_j \right] dt, (i, j = 1, 2, 3),
 \end{aligned} \tag{10}$$

see *e.g.* Jameson, Schmidt and Turkel (1981) [31] for more information.

To solve the pressure -velocity coupling in Eq. (10), There are three popular algorithms that can be employed, namely the Pressure Implicit Splitting Operator (PISO) algorithm, the Semi-Implicit Method for Pressure-Linked equations (SIMPLE) algorithm and the PISO-SIMPLE (PIMPLE) algorithm. In PIMPLE algorithm, the SIMPLE algorithm are employed to iteratively calculate pressure from velocity component in the Navier-Stokes (NS) equations and the PISO algorithm is employed to revise the results, see Issa (1986) [32] and Ferziger *et al.* (2012) [33]. The PIMPLE algorithm is time saving because a larger Courant number ($C_r \gg 1$) can be used. PIMPLE do not show too much advantages in simple cases and flow patterns. For more complicated geometries, skewed, non-orthogonal meshes, PIMPLE can stabilize the simulations whereas the case may fail or cost too much time with PISO and SIMPLE, see Holzmman (2016) [34].

The free surface is determined by use of the volume of fluid method. The computations are carried out using an open source computational software, namely OpenFOAM.

The GN equations are solved by use of a central difference scheme, second order in space, and by use of the modified Euler's method for time marching. See Ertekin (1984) [21] and Ertekin, Webster and Wehausen (1986) [35] for discussion on the solution of the Level I the GN equations as used here.

The SV equations are solved by use of a finite volume method. The integral form of Eq. (6) over time and space

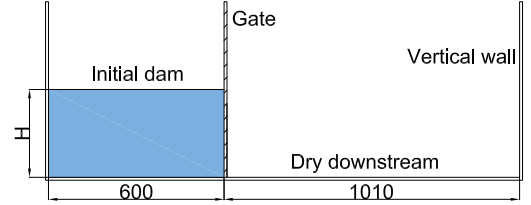


FIGURE 1: Schematic of the dam-break experimental tank of Lobovský *et al.* (2014) [10] used for the comparison purposes. The unit is in mm.

can be written as:

$$\begin{aligned}
 \int_t^{t+\Delta t} \int u_{1,i} dx_1 + \int u_1 \partial u_{1,1} dx_1 \Big|_t^{t+\Delta t} &= \int_t^{t+\Delta t} \left[\int -gh_{,1} dx_1 \right. \\
 &\quad \left. + \int gS - gS_{f,1} dx_1 \right] dt.
 \end{aligned} \tag{11}$$

Details of the computational model of the SV equations as used here can be found in Morris (2013) [36].

Numerical Setup

A grid convergence study is performed to determine the appropriate grid for the computations. Here, we only present the grid convergence of the RANS equations. The convergence test of the GN and the SV equations can be found in *e.g.* Ertekin *et al.* (2014) [37] and Morris (2013) [36], respectively. For the grid convergence study of the RANS model, we consider the experiment of Lobovský *et al.* (2014) [10].

In the experiments of Lobovský *et al.* (2014) [10], a tank, 1,610 mm long, 600 mm high and 150 mm wide is used. The reservoir is on the left, and the gate is 600 mm away from the upstream wall of the tank, as shown in Fig.1. The initial dam height is $H = 300$ mm. The gate opens at $t = 0$ s, and bore propagates toward downstream and hits the downstream wall. Five pressure sensors are placed at the downstream wall to record the bore pressure. The locations of the sensors, S_1 - S_5 , are shown in Fig. 2. More details about the experiment is given in the following sections.

For the RANS computations, two Intel®Xeon E5-2697A v4 processor (16 cores, 40 M Cache, 3.00GHz) are used. Maximum Courant Number is 0.25 and average

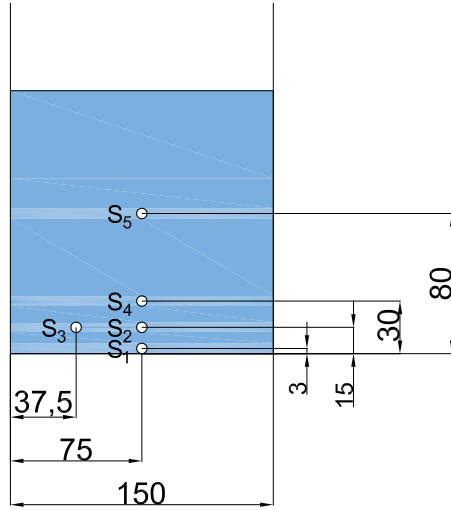


FIGURE 2: A front view showing the location of pressure sensors on the impact wall downstream the tank. The unit is in mm.

TABLE 2: Grid information of the convergence tests of the 2D RANS equations.

Grid ID	$\Delta x_1/h$	$\Delta x_2/h$	number of cells		Computation duration(hr)
			x_1	x_2	
1	0.0008	0.0008	2013	750	2.74
2	0.001	0.001	1610	600	1.12
3	0.0012	0.0012	1342	500	0.51
4	0.0014	0.0014	1150	429	0.29

Courant Number is 0.0086. Four uniform grids are considered in this part which are summarized in Table 2. The RANS model for the grid convergence study is performed in two dimensions only. The distribution of the pressure on the downstream wall are studied in five pressure sensors for these grids. Comparisons of pressure time series on the downstream wall of the four grids are shown in Fig. 3. Results are given in dimensionless form using ρ , g and H or h as a dimensionally independent set. For the dam-break problems, $p' = p/\rho g H$ and $t' = t\sqrt{g/H}$, where H is the initial dam height, shown in Fig. 1. For the initial mound of water problem, $p' = p/\rho g h$ and $t' = t\sqrt{g/h}$, where h is the downstream water level, shown in Fig. 6.

From this grid study, we determine that Grid 3 ($\Delta x_1/h = \Delta x_2/h = 0.0012$) can be used for this problem. The grids used by all models for the problems studied here are listed in Table 3.

Results and Discussion

Bores generated by breaking of a dam and initial mound of water are studied here. The fundamental difference be-

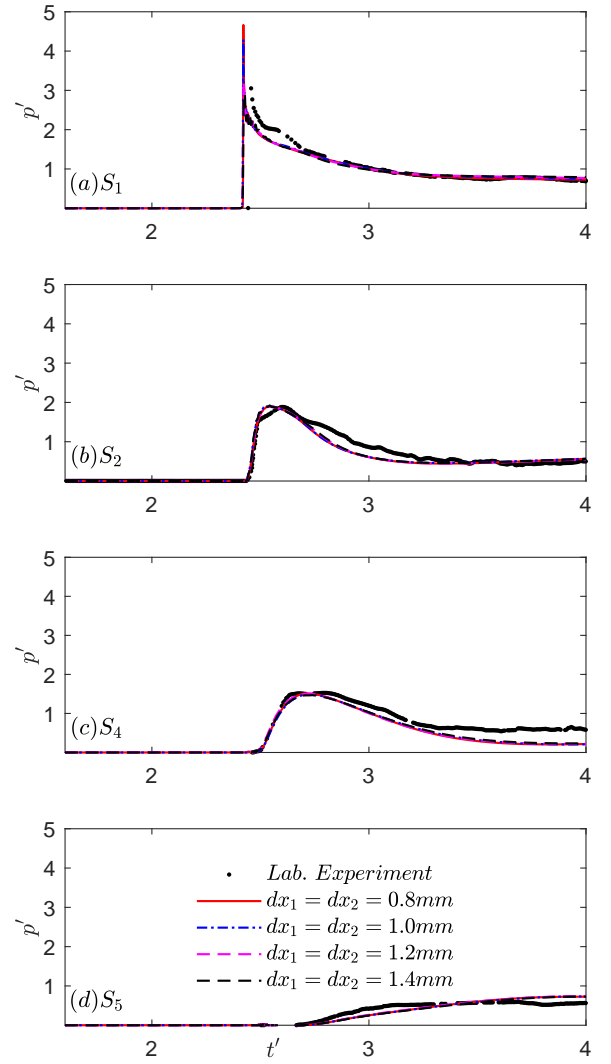


FIGURE 3: The grid convergence study of the RANS equations: comparisons of pressure recorded by Sensors S_1 , S_2 , S_4 and S_5 computed by the RANS equations vs laboratory measurements of Lobovský *et al.* (2014) [10].

TABLE 3: Grid size of the cases studied in this work. N/A stands for not applicable.

model	$\Delta x_1/h$	$\Delta x_2/h$
RANS equations	0.0012	0.0012
GN equations	0.03	N/A
SV equations	0.001	N/A

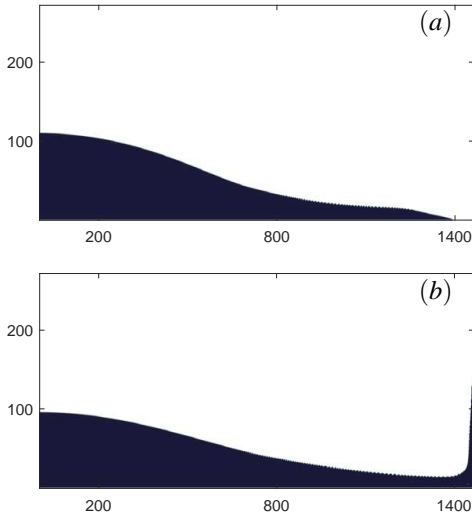


FIGURE 4: Snapshots of (a) the bore at $t' = 2.29$ ($t = 0.4s$) and (b) at $t' = 2.86$ ($t = 0.5s$).

tween these cases is the downstream water depth; in the dam break problem, down stream is either dry or the water depth is much smaller than the initial mound of water. We first consider the dam break case and the experiments carried out by Lobovský *et al.* (2014) [10]. The NS and SV equations are used to study the dam break problem. This is followed by discussion of the initial mound of water problem, where downstream water depth is larger than the initial height of the reservoir (above the SWL).

Bore Generated by Dam Break

Simulations of the three dimensional experiment of Lobovský *et al.* (2014) [10] is first presented. The tank used in the experiment is shown in Fig.1. The initial dam height is $H = 300mm$. There are five pressure sensors at the downstream wall. The locations of the sensors, S_1 - S_5 , are shown in Fig. 2.

Shown in Fig. 2, sensor S_3 is used to study the three dimensionality effect. All results are presented in dimensionless form. The experimental data of Lobovský *et al.* (2014) [10] are given in dimensionless quantities with respect to the constant initial dam height (H), water density (ρ), and the gravitational acceleration (g).

The RANS computations are carried out in both 2D and 3D, for comparison purposes. The grid size in x_1 and x_2 directions of the 3D computations, used the 3D RANS equations, are the same with that of the 2D RANS equations, see Table 2. The grid size in x_3 (into the page) is $\Delta x_3/h = 0.0012$ and the number of cells in x_3 direction is 125. The 3D RANS computations were completed in 478 hours.

Snapshots of the bore propagations, determined by the 2D RANS equations, are presented in Fig. 4 for two times: (upper) bore shape before it arrives at the downstream wall, and (lower) bore shape as it hits the downstream wall.

The pressure on the downstream wall computed by the 3D RANS equations, the 2D RANS equations and SV equa-

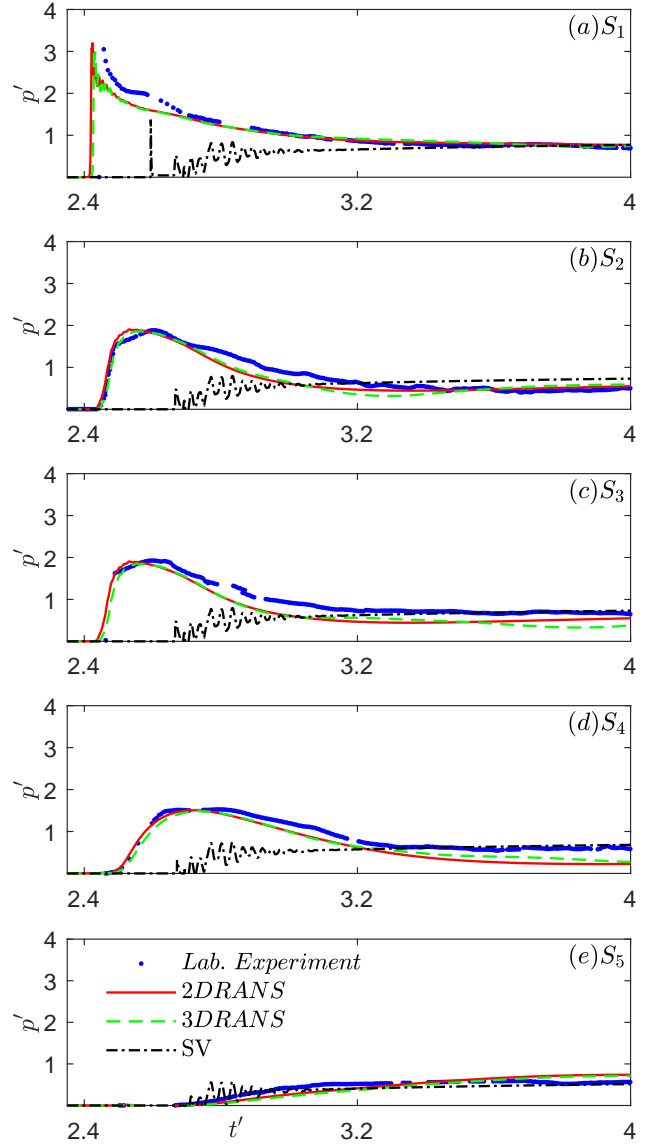


FIGURE 5: Comparisons of bore pressure time series between experimental measurement of Lobovský *et al.* (2014) [10], the 2D RANS equations, 3D RANS equations and SV equations at Sensors (a) S_1 , (b) S_2 , (c) S_3 , (d) S_4 and (e) S_5 .

tions are compared with the experimental data in Figs. 5. The pressure at Sensor S_3 , shown in Fig. 5(c) of the 2D RANS equations is the same with that at Sensor S_2 .

Figure 5(a) shows the pressure at Sensor S_1 has a sudden jump to the highest value when the bore arrives at the downstream wall and decreases gradually after that. Good agreement is observed between the 2D and the 3D RANS equations and the experimental data. The pressure at Sen-

sor S_1 computed by the SV equations jump to the highest value when the bore arrives at the downstream wall, drops to a small value and increases slowly with fluctuations before $t' = 3.0$. The bore speed determined by the SV equations is significantly smaller than others, and the maximum pressure magnitude is underestimated. The difference of the results between the SV equations and others is due to the assumptions made in deriving the SV equations. The bore propagation along the downstream wall, is underestimated by the SV equations, so the pressure computed by the SV equations drop to a small value.

The bore, computed by 2D and the 3D RANS equations, reach Sensor S_1 at $t' = 2.415$ and $t' = 2.421$, respectively, and at $t' = 2.592$ for the SV equations and at $t' = 2.445$ for the experiments. The slight difference between the 2D RANS equations and 3D RANS equations in bore propagation speed is due to the effect of the left and right wall of the tank in the 3D RANS equations simulation. The SV equations have underestimated the bore propagation speed and pressure, due to the assumptions made.

Figures 5(b), 5(c) and 5(d) show the pressures of Sensors S_2 , S_3 and S_4 , respectively. At Sensors S_2 , S_3 and S_4 , pressure of the laboratory experiment and the pressure computed by the 2D RANS equations and 3D RANS equations increases to highest value then decreases gently, while the pressure computed by the SV equations increases with large fluctuations before and at a later time $t' = 3.0$.

There is little difference between the pressure of the 2D RANS equations and 3D RANS equations before $t' = 3.0$. After that time, some differences can be seen in Figs. 5(b), 5(c) and 5(d). In the snapshots shown in Fig 4, taken at $t' = 2.86$, the bore almost reaches the highest level on the wall and is going to returns towards upstream. Larger differences are seen between the pressure of the 2D RANS equations and 3D RANS equations at this point, as the resistance from the front and back walls on the bore is significant. Hence, it appears that the 2D RANS equations model can be safely used to study the pressure on downstream wall before the bore reaches the highest level.

Figure 5(e) shows the pressure at Sensors S_5 . At Sensors S_5 , the pressure of the experiment and the pressure computed by the 2D RANS equations and 3D RANS equations increase gently without experiencing a peak. This is because the horizontal bore speed is smaller at the position of Sensor S_5 , when compared to the other sensors. The pressure computed by the SV equations increase with fluctuations.

The pressures on the downstream wall computed by the 2D RANS equations and 3D RANS equations agree well with the pressure peak measured by the five sensors in the laboratory experiment of Lobovský *et al.* (2014) [10].

The pressures computed by the 2D RANS equations are closer to the experimental data than that of the SV equations. The SV equations cannot capture the sudden change in bore propagation and hence the pressure.

Bore Generated by Initial Mound of Water

In this section, we study the bore generation, propagation and pressure due to an initial mound of water. The significant difference of this case, when compared to the dam-break problem, is due to the downstream water depth. Computations of this section is in two dimensions.

A schematic of the numerical tank is shown in Fig. 6. Note that in the case of an initial mound of water, $A < h$, where A is the water height (above the SWL) at the reservoir. The RANS, GN and SV models are used in this section. The length of the computational domain is defined such that the computations stop before waves arrive at the downstream boundary.

At time $t = 0$, water is at rest. After that, gate at $x_1 = L$ is removed instantly and completely. Several solitons are generated and move towards downstream without significant change in wave height, details can be seen in *e.g.* Ertekin, Hayatdavoodi and Kim (2014) [37]. We consider a case with initial mound amplitude, $A = 0.4h$, and initial length, $L = 12h$. Six pressure sensors and six wave gauges are located on the tank floor to measure the pressure on the base. The locations of the gauges and sensors are shown in Fig. 6.

The GN computations are carried out for dimensionless variables with respect to the downstream water depth. The downstream water depth, $h = 1m$ is constant in the RANS and the SV computations.

The snapshots of the surface elevation computed by the RANS equations, the GN equations and the SV equations at $t' = 30, 50$ are shown in Fig. 7. The vertical axis shows the surface elevation of water. The results of the computational models are in close agreement for the leading solitons, but the results of the SV equations lose the details and has only provided the average.

The pressures on the tank floor computed by the RANS equations and the SV equations are compared with that of the GN equations in Fig. 8. The bore pressure is recorded by six sensors located on the tank floor. The sensors are labelled $S1-S6$ and are shown in Fig. 6. Also shown in Fig. 8 is the surface elevation recorded at wave gauges located exactly above the pressure sensors.

Figure 8(a) and Fig.8(g) show the surface elevations of gauge G_1 and the pressure at Sensor S_1 , respectively, computed by the GN equations, RANS equations and SV equations. Overall, results of the RANS and GN equations are in close agreement, while the SV equations have simplified the solution. The surface elevation and pressure computed by the GN equations show larger fluctuations than the results of the RANS equations. The reason of this should be due to the numerical fluctuation found near the gate, see Fig.7.

Figures 8(b)-8(f) and 8(h)-8(l) show the surface elevations of Gauges $G_2 - G_6$ and pressures of Sensors $S_2 - S_6$, respectively, computed by the GN equations, RANS equations and SV equations. Results are in good agreements. The results of the GN equations do not shows the fluctuations any more for the gauges and sensors are far from the gate.

Overall, the surface elevation and pressure computed by the GN equations show good agreement with results of the

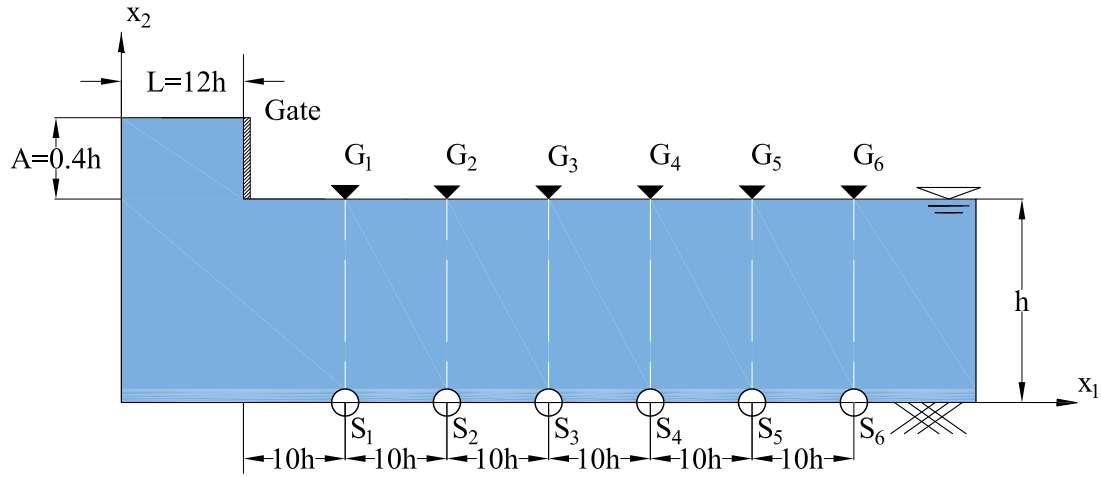


FIGURE 6: Schematic of the numerical tank of the initial mound of water problem and location at the wave gauges and the pressure sensors. Not to scale.

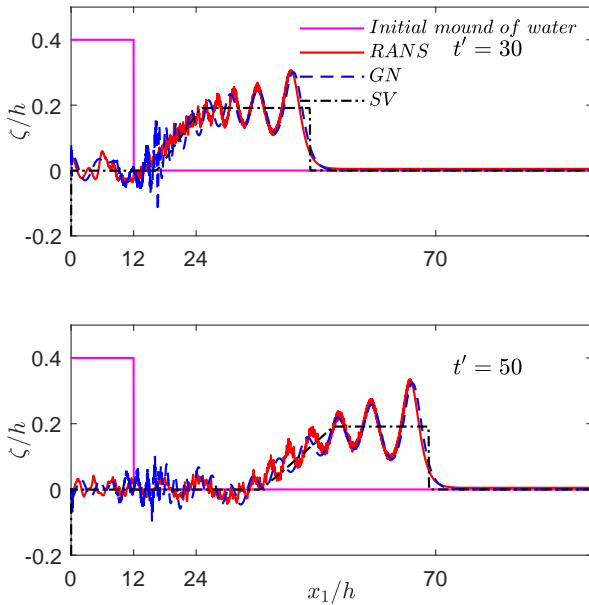


FIGURE 7: Snapshots of the computational model at different time. ($A = 0.4h$, $L = 100h$)

RANS equations, while the SV equations only provide average information. The SV equations and GN equations appear to show less sensitivity to the pressure than the RANS equations. The bottom pressure shows close relation with the free-surface fluctuations. So hydrostatic pressure is the main component of the bottom pressure when initial mound of water problem is studied.

Concluding Remarks

The 2D RANS equations, the 3D RANS equations and the SV equations are used to study the dam-break problem,

where initial height of the water is much larger than the downstream water depth. The pressure on the downstream wall of these three models are compared with laboratory experiments.

It is found that the pressures computed by the 2D RANS equations and 3D RANS equations agree well with each other before the bore reaches the highest point on the downstream wall. The boundary conditions of the front and back walls in the 3D RANS equations is one of the reasons for slight differences after that point. Moreover, in the 3D model, the bore can propagate into the page direction after it hits the vertical wall. So the pressure during this period computed by the 3D model is slightly different from that of the 2D model. As the 3D model is computationally more costly, 2D model is suggested when the interest is confined to the pressure before bore approaches the highest point on the downstream wall.

Pressure computed by the SV equations agrees well with the RANS equations and experimental data when the pressure sensor is high enough on the wall. But the SV equations underestimate the bore height and speed and hence shows less sensitivity with the sudden change of water height. In the SV equations, pressure distribution is simplified by hydrostatic distribution and the momentum direction is restricted to one dimension.

The pressure peaks computed by 2D and the 3D RANS equations agree well with the experimental data, although there are slight differences in the time of the pressure peak. The maximum pressure results provided by the RANS equations seems to be acceptable for engineering applications.

The RANS equations, GN equations and SV equations are used to study the generation, propagation and pressure of an initial mound of water. The equations show close agreement for the generation and propagation of bore of initial mound of water. The results of the SV equations has significantly lost the details.

Overall, close agreement is observed between the results of the RANS equations, GN equations and SV equations.

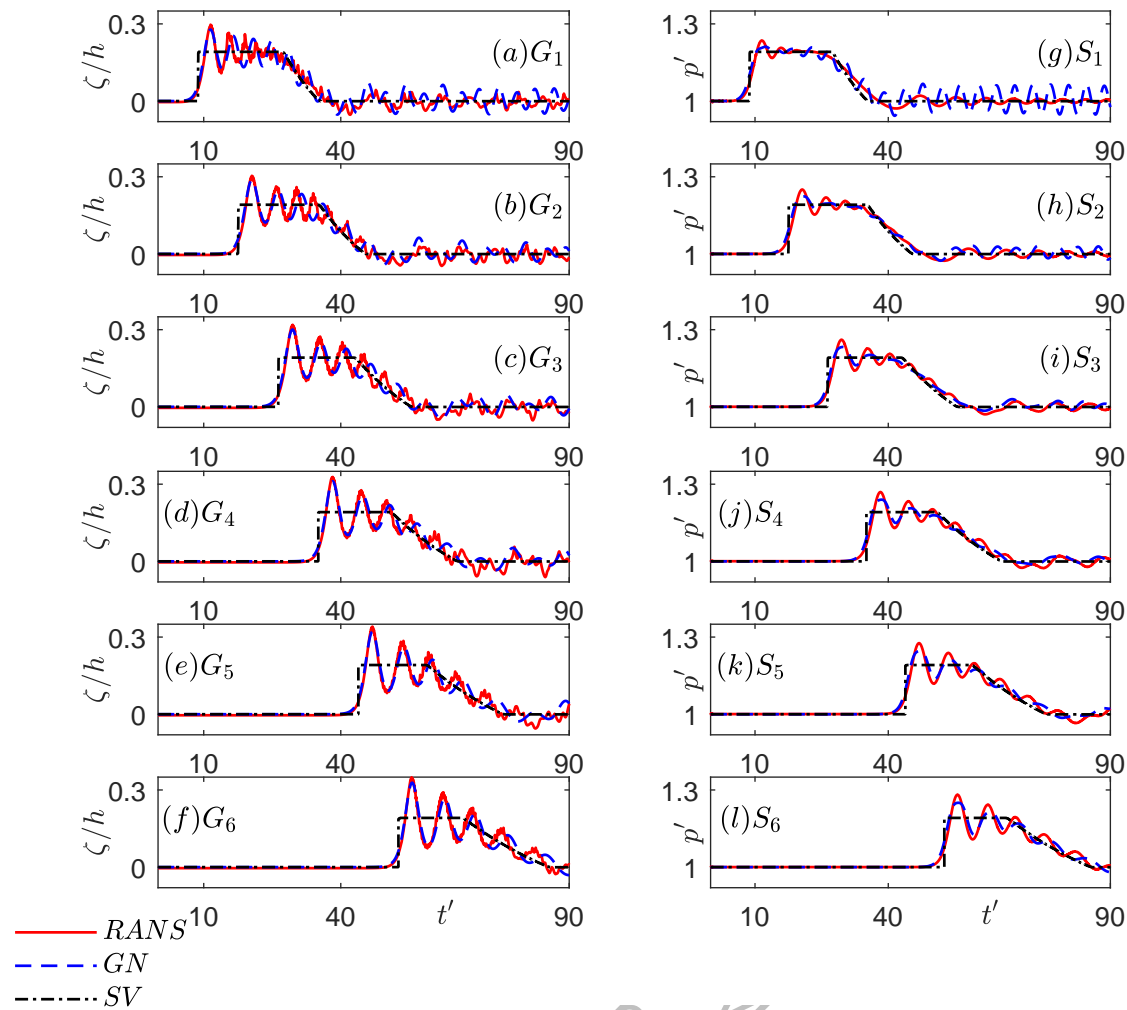


FIGURE 8: Comparison of the surface elevation between the RANS equations, the GN equations and the SV equations at Gauges (a) G_1 , (b) G_2 , (c) G_3 , (d) G_4 , (e) G_5 and (f) G_6 and the pressure between the RANS equations, the GN equations and the SV equations at Sensors (g) S_1 , (h) S_2 , (i) S_3 , (j) S_4 , (k) S_5 and (l) S_6 . ($A = 0.4h$, $L = 12h$)

tions. Given that the computational cost of the GN equations (often less than a minute) is much less than that of the RANS equations, the GN equations appear to be a good substitute to the RANS equations in these cases. In the GN equations, however, the function ζ (surface elevation) is single-valued. Hence, application of the GN equations is limited to cases that do not involve wave breaking or dry seabed.

REFERENCES

- [1] Pilotti, M., Maranzoni, A., Tomirotti, M., and Valerio, G., 2010. "1923 Gleno dam break: Case study and numerical modeling". *Journal of Hydraulic Engineering*, **137**(4), pp. 480–492.
- [2] Seed, H. B., and Duncan, J. M., 1981. "The teton dam failure—a retrospective review". In *Soil mechanics and foundation engineering: proceedings of the 10th international conference on soil mechanics and foundation engineering*, Stockholm, Sweden, pp. 15–19.
- [3] Yalciner, A. C., Perincek, D., Ersoy, S., Presateya, G., Hidayat, R., and McAdoo, B., 2005. "Report on December 26, 2004, Indian Ocean Tsunami, Field Survey on Jan 21–31 at North of Sumatra".
- [4] West, M., Sánchez, J. J., and McNutt, S. R., 2005. "Periodically triggered seismicity at Mount Wrangell, Alaska, after the Sumatra earthquake". *Science*, **308**(5725), pp. 1144–1146.
- [5] Ritter, A., 1892. "Die fortpflanzung der wasserwellen". *Zeitschrift des Vereines Deutscher Ingenieure*, **36**(33), pp. 947–954.
- [6] Hu, C., and Kashiwagi, M., 2004. "A CIP-based method for numerical simulations of violent free-surface flows". *Journal of Marine Science and Technology*, **9**(4), pp. 143–157.
- [7] Zhou, Z., De Kat, J., and Buchner, B., 1999. "A non-linear 3d approach to simulate green water dynamics on deck". In *Proceedings of the Seventh Interna-*

- tional Conference on Numerical Ship Hydrodynamics, Nantes, France, pp. 1–15.
- [8] Kleefsman, K., Fekken, G., Veldman, A., Iwanowski, B., and Buchner, B., 2005. “A volume-of-fluid based simulation method for wave impact problems”. *Journal of computational physics*, **206**(1), pp. 363–393.
 - [9] Wemmenhove, R., Gladsø, R., Iwanowski, B., and Lefranc, M., 2010. “Comparison of CFD calculations and experiment for the dambreak experiment with one flexible wall”. In The Twentieth International Offshore and Polar Engineering Conference, Beijing, China, International Society of Offshore and Polar Engineers.
 - [10] Lobovský, L., Botia-Vera, E., Castellana, F., Mas-Soler, J., and Souto-Iglesias, A., 2014. “Experimental investigation of dynamic pressure loads during dam break”. *Journal of Fluids and Structures*, **48**, pp. 407–434.
 - [11] Wilcox, D. C., 1998. *Turbulence modeling for CFD*, Vol. 2. DCW industries La Canada, CA.
 - [12] Mokrani, C., and Abadie, S., 2016. “Conditions for peak pressure stability in vof simulations of dam break flow impact”. *Journal of Fluids and Structures*, **62**, pp. 86–103.
 - [13] Menter, F. R., 1993. “Zonal two equation $k - \epsilon$ turbulence models for aerodynamic flows”. In 23rd Fluid Dynamics, Plasmadynamics, and Lasers Conference, Orlando, Florida, U.S.A, pp. 1–21.
 - [14] Menter, F. R., Kuntz, M., and Langtry, R., 2003. “Ten years of industrial experience with the SST turbulence model”. *Turbulence, heat and mass transfer*, **4**(1), pp. 625–632.
 - [15] Hirt, C. W., and Nichols, B. D., 1981. “Volume of fluid (VOF) method for the dynamics of free boundaries”. *Journal of Computational Physics*, **39**(1), pp. 201–225.
 - [16] Greenshields, C. J., 2018. “OpenFOAM user guide”. *OpenFOAM Foundation Ltd, version*, **3**(1).
 - [17] Higuera, P., Lara, J. L., and Losada, I. J., 2013. “Realistic wave generation and active wave absorption for Navier–Stokes models: Application to OpenFOAM®”. *Coastal Engineering*, **71**, pp. 102–118.
 - [18] Green, A. E., Laws, N., and Naghdi, P. M., 1974. “On the theory of water waves”. *Proc. R. Soc. Lond. A*, **338**(1612), pp. 43–55.
 - [19] Green, A. E., and Naghdi, P. M., 1976. “Directed fluid sheets”. *Proceedings of the Royal Society of London*, **347**(1651), pp. 447–473.
 - [20] Green, A. E., and Naghdi, P. M., 1976. “A derivation of equations for wave propagation in water of variable depth”. *Journal of Fluid Mechanics*, **78**(2), pp. 237–246.
 - [21] Ertekin, R. C., 1984. “Soliton generation by moving disturbances in shallow water: theory, computation and experiment”. PhD thesis, University of California at Berkeley.
 - [22] Hayatdavoodi, M., and Ertekin, R. C., 2015. “Non-linear wave loads on a submerged deck by the green–naghdi equations”. *Journal of Offshore Mechanics and Arctic Engineering*, **137**(1), p. 011102.
 - [23] Hayatdavoodi, M., and Ertekin, R. C., 2015. “Wave forces on a submerged horizontal plate. Part I: Theory and modelling”. *J. of Fluids and Structures*, **54**(April), pp. 566–579.
 - [24] Hayatdavoodi, M., and Ertekin, R. C., 2015. “Wave forces on a submerged horizontal plate. Part II: Solitary and cnoidal waves”. *J. of Fluids and Structures*, **54**(April), pp. 580–596.
 - [25] Neill, D. R., Hayatdavoodi, M., and Ertekin, R. C., 2018. “On solitary wave diffraction by multiple, in-line vertical cylinders”. *Nonlinear Dynamics*, **91**(2), pp. 975–994.
 - [26] Hayatdavoodi, M., Neill, D. R., and Ertekin, R. C., 2018. “Diffraction of cnoidal waves by vertical cylinders in shallow water”. *Theoretical and Computational Fluid Dynamics*, **32**(5), pp. 561–591.
 - [27] Saint-Venant, A. d., 1871. “Theorie du mouvement non permanent des eaux, avec application aux crues des rivières et à l’introduction de marées dans leurs lits”. *Comptes rendus des seances de l’Academie des Sciences*, **36**, pp. 147–237.
 - [28] Mises, R. V., 1945. “On Saint Venants principle”. *Bulletin of the American Mathematical Society*, **51**(8), pp. 555–562.
 - [29] Manning, R., 1889. “On the flow of water in open channels and pipes”. *Institution of Civil Engineers of Ireland*, **20**, pp. 161–207.
 - [30] Kundu, P., and Cohen, L., 1990. *Fluid mechanics*. Academic Press.
 - [31] Jameson, A., Schmidt, W., and Turkel, E., 1981. “Numerical solution of the Euler equations by finite volume methods using Runge Kutta time stepping schemes”. In 14th fluid and plasma dynamics conference, Palo Alto, California, U.S.A., p. 1259.
 - [32] Issa, R. I., 1986. “Solution of the implicitly discretised fluid flow equations by operator-splitting”. *Journal of computational physics*, **62**(1), pp. 40–65.
 - [33] Ferziger, J. H., and Peric, M., 2012. *Computational methods for fluid dynamics*. Springer Science & Business Media.
 - [34] Holzmann, T., 2016. Mathematics, numerics, derivations and openfoam®.
 - [35] Ertekin, R. C., Webster, W. C., and Wehausen, J. V., 1986. “Waves caused by a moving disturbance in a shallow channel of finite width”. *Journal of Fluid Mechanics*, **169**, pp. 275–292.
 - [36] Morris, A. G., 2013. “Adapting cartesian cut cell methods for flood risk evaluation”. PhD thesis, Manchester Metropolitan University.
 - [37] Ertekin, R. C., Hayatdavoodi, M., and Kim, J. W., 2014. “On some solitary and cnoidal wave diffraction solutions of the Green-Naghdi equations”. *Applied Ocean Research*, **47**, pp. 125–137.